Journal of Sol-Gel Science and Technology (2022) 104:276–286
https://doi.org/10.1007/s10971-022-05935-5

ORIGINAL PAPER: FUNDAMENTALS OF SOL-GEL AND HYBRID MATERIALS PROCESSING

Linking rheology, process parameters and formability for material extrusion and photo-polymerization combined process aiming at high-density ceramics

Xin He[1] · Jie Xu[2] · Weixi Ji[1]

Received: 8 June 2022 / Accepted: 3 September 2022 / Published online: 26 September 2022

Abstract

Material extrusion and photo-polymerization (MEX-PPM) process is a great potential for ceramic components in the aerospace field, while the uncertain formability of ceramic parts and rheological property of slurry limit its further application. In this work, using spherical alumina powder with particle size of 1 μm, prepolymer 1, 6-hexanediol diacrylate, surfactant oleic acid and photo-initiator diphenyl (2, 4, 6-trimethylbenzoyl) phosphate oxide as raw material, a series of 60wt % and 70wt % Al_2O_3 ceramic slurry with different viscosities were obtained by aging, and their comprehensive properties such as the rheology, flow behavior and formability through experiments were evaluated. The comprehensive forming model linking formability and rheology of slurry, process parameters such as printing speed and radiation power was established. The results showed that the predicted dimension (D_{pre}) and printing dimension (D_p) of the green body formed by adjusting the process parameters were close to each other. The printing speed and radiation power were adjusted to 5 mm/s and 23.5 J/s, respectively. The D_p and D_{pre} were approximated to design dimension (D_d) of the green body formed using 70wt % slurry. The internal structure of sintered body was uniform without obvious defects, the density could reach at 96.2% (theoretical density of 3.96 g/cm^3), and the hardness was at 15.67 GPa. In sum, the effectiveness of this new model was proved, and the dense ceramic structures could be formed well by regulating parameters of MEX-PPM process under the limited slurry rheology.

Graphical abstract

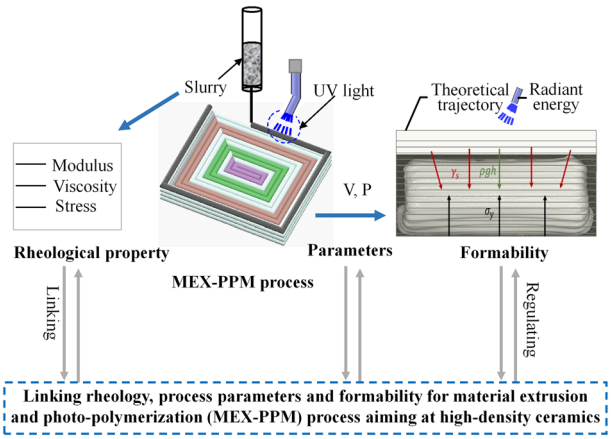

✉ Jie Xu
xujiemechanic@163.com

✉ Weixi Ji
weixiji_jiangnan@outlook.com

[1] School of Mechanical Engineering, Jiangnan University, Wuxi 214122, China

[2] Department of Astronautical Science and Technology, Space Engineering University, Beijing 101400, China

Keywords Material Extrusion · Photo-polymerization · High-density · Al_2O_3 Ceramic

Highlights

- A comprehensive forming model of material extrusion and photo-polymerization combined (MEX-PPM) process was built.
- The comprehensive model can guide the design of slurry and set printing speed and radiation power for various 3D printing process.
- The compact ceramics with good formability were produced using MEX-PPM process by adjust the parameters of model.

1 Introduction

Ceramic 3D printing technology is based on discrete-collecting principle, driven by three-dimensional data of parts, and layer-by-layer depositing materials directly forming objects. This technology has the advantages of free design, rapid prototyping and good economy [1–3], and is known as one of the key technologies leading the 3rd industrial revolution [4, 5]. Therefore, the perfect ceramic 3D printing process should be able to satisfy the forming requirements of ceramic parts with specific geometric accuracy, density and multi-material distribution [6–8]. Since the forming of ceramic parts is synergistically influenced by the rheology of ceramic slurry, the process parameters such as printing speed, radiation power, etc. [9–11], it is necessary to define the relationship between them.

According to the principle of 3D printing technology, the printing processes used in research on printability of ceramic can be divided into three categories which including material extrusion (MEX) process, photo-polymerization (PPM) process, material extrusion and photo-polymerization combined (MEX-PPM) process. The MEX process requires that the ceramic slurry can be easily extruded through a small diameter nozzle and the slurry needs sufficient yield force to resist deformation immediately after extrusion. Enlarging the nozzle diameter is beneficial to printing of MEX process, but it will lead to low resolution and poor compactness [12–14]. The previous study has assessed slurry rheology and printability [15], proving that the rheology was affected by viscoelasticity and yield stress simultaneously, and they could not be regulated separately [16–18]. Compared with MEX process, the PPM process can provide UV light curing photosensitive slurry, and inhibit more effectively on the deformation of green body. The UV radiation energy can be adjusted independently to adapt process parameters such as printing speed and nozzle diameter, but the PPM process was limited for not producing multi-material structures [19–21]. The MEX-PPM process [22] provides a new method for producing multi-material and dense ceramic parts. As a novel method, the regular between the rheology of slurry, the process parameters and formability of part is required to be deeply studied.

Recently, a series of attempts have been carried out to improve the printability of ceramic slurry. M Barki et al. [23] defined a dimensionless parameter by an equation that contains variables including rheological parameters such as density, dynamic yield force and surface tension, nozzle dimension and component height, and connected the rheology and printability of the Al_2O_3 slurry used in the direct ink writing (DIW) process to quantify the component collapse deformation. The relative density and bending strength of the part are 97% and 281–858 MPa, respectively. However, the higher value of deformation will cause interlayer defects and lower density value. Hence, it is difficult to ensure the high relative density and forming accuracy of the ceramic part at the same time. Li et al. [24] studied the synergy between the solid content of Al_2O_3 slurry and the printability for a stereo-lithography (SLA) process, and the results showed that solid content increases viscosity of the slurry, reduces the shrinkage rate of green body and improves the relative density of sintered parts. However, when the solid content was higher than 52 vol %, processing defects such as poor interlaminar bonding, surface cracks, etc., which may be caused by high radiation energy or poor slurry fluidity. Chen et al. [25] also studied the processability based on PPM process of cordierite ceramic slurry, where surfactants (Optimal content 5wt %) and ceramic particle size were found to affect the slurry viscosity, the photoinitiator was found (optimal content 2wt %) to affect the photocuring behavior. Although curing thickness of photosensitive slurry increased with the increase of radiation energy, and decreased with the increase of solid content, there is no further analysis on the effects of radiation energy and viscosity of slurry on the forming parts. M. Rosa et al. [26] designed a yttria stabilized zirconia (YSZ) ink for the inkjet-SLA combined process, which overcome the low density and poor resolution of the green body prepared by MEX process, and the PPM process can only print single material structure. The effects of solid content and UV monomer on rheological and photocuring behavior were studied respectively. YSZ

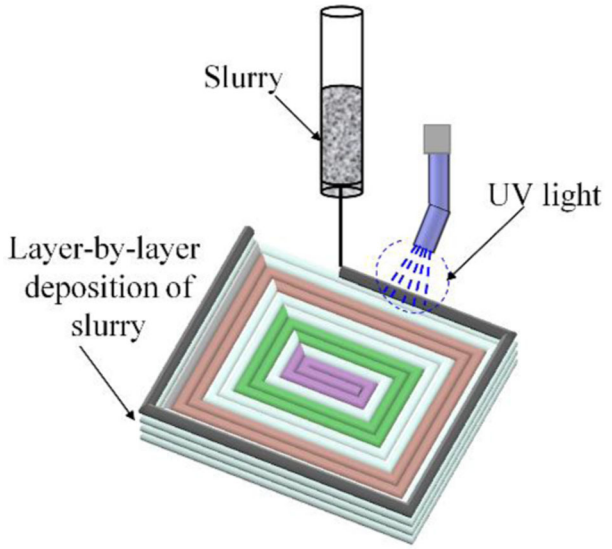

Fig. 1 Process diagram of ceramic parts prepared by MEX-PPM process

ceramics with relative density of 96% were obtained. Although the above studies have analyzed the effects of the rheology or photocuring behavior of ceramic slurry on printed parts, it is insufficient to improve the quality only by adjusting either of them. The linking rheology of slurry, radiation energy, printing speed and formability should be discussed furtherly.

In this work, Al_2O_3 photosensitive ceramic slurry with high solid content and low viscosity were prepared, the rheology of slurry under different aged conditions were characterized. The deformation of green body printed by MEX-PPM process was quantified, and the comprehensive forming model of the green body was established. The dimension of green body based on the comprehensive forming model, as well as the density, mechanical properties and microstructure of sintered body were analyzed. According to the experimental results, the effectiveness of the comprehensive forming model in MEX-PPM process printing ceramic green body was evaluated.

2 Experimental details

2.1 Materials

The ceramic powder used in this study was spherical alumina (Al_2O_3) with theoretical density of 3.96 g/cm^3 and particale size of 1 μm (Dongfeng Metal Research Center, China). It has good mechanical properties, chemical stability and economy. 1, 6-hexanediol diacrylate (HDDA) (Changxing Chemical Co., China) with low viscosity and easy curing was used as the prepolymer, oleic acid (OA) with amphoteric groups as surfactant to modify Al_2O_3 particles with hydrophilic groups on the surface to improve the solubility of alumina in the prepolymer. Diphenyl (2, 4, 6-trimethylbenzoyl) phosphate oxide (TPO) (BASF GmbH, Germany) was used as photo-initiator.

2.2 Experimental methods

2.2.1 Preparation of photosensitive ceramic slurry

Firstly, Al_2O_3 powder was added into ethanol containing 0.15wt % OA, milled by planetary stirring ball mill (QM-3SQ4, Nanjing Nanda instrument Co., China) for 6 h, dried at 80 °C in the vacuum drying oven (DZF-6020, Shanghai Suoyan Test Equipment Co., China), and sieved through 80 mesh screen to obtain OA-modified Al_2O_3 powder. The OA-modified Al_2O_3 powder was then added into the HDDA prepolymer solution containing 1wt % TPO, and ground with a planetary mill at 400 rpm for 4 h. The bubbles in the slurry were removed by vacuum ultrasonic vibration. Two groups of 60wt % and 70wt % slurry were prepared by the above process and the ageing in closed vessel at room temperature for 0–480 h, in which the completion time of slurry was defined as the $t_{aging} = 0$.

2.2.2 Forming of ceramic green body

In this study, ceramic green bodies were produced by the MEX-PPM and used to evaluate the formability. According to the parameters of TPO in raw materials, the UV light with wavelength of 405 nm was used in the printing process. The process of printing green body by MEX-PPM is shown in Fig. 1.

The 3D printing equipment that implements the MEX-PPM process is our previous work [27], which mainly consists of base, precision three-axis motion platform, extrusion control device, forming device and curing light source device. In the process of green body printed by MEX-PPM process, the worktable connected with the three-axis platform moves in X, Y and Z directions, and the slurry in the fixed position storage barrel is deposited layer by layer from left to right along the planned path through a circular nozzle, while the shape is maintained by UV light irradiation. The diameter of the round nozzle used is 0.25 mm and 0.5 mm, the printing speed is 0–7 mm/s, the power of UV lamp (MZLASER, China) is 0–150 W, and the power supply voltage is 2.8–12 V. In the printing process, the appropriate printing speed and radiation power can be adjusted according to the performance of the slurry to prepare the perfect green body, which will be discussed in Section 3. The above processes were carried out at room temperature of 25 ± 0.05 °C using DC electrical source.

2.3 Characterization

Rheology tests were performed on 60wt % and 70wt % slurry of different aging time using the rotary rheometer (DHR-2, TA Instruments, USA) to evaluate its rheological properties, using a 25 mm parallel plate geometry and PEG heat-exchanger stabilized the temperature at 25 ± 0.05 °C and points per decade 5. For stress vs. shear rate cyclic flow curve, the shear rate ramp-up followed by ramp-down from 0 s^{-1} to 120 s^{-1} without time interval at same conditions. The other stress and viscosity were obtained by flow sweep in (100–10^2) s^{-1}. The shear modulus (Elastic modulus and viscous modulus) at plateau values in the linear viscoelastic region were obtained by oscillation amplitude at sampling frequency of 1 Hz in stress of (0.1–σ_y) Pa.

The surface tension of slurry was measured by pendant drop method in automatic surface tensiometer (DCAT21, Germany). During the test, the ceramic slurry was suspended on a round-hole nozzle with a diameter of 1.37 mm. Images were taken by a high-intensity backlight digital microscope and obtained by image processing software (Image J) for the final surface tension. A 3D video microscope (KH-8700, HIROX Co., Japan) was used to obtain the printing dimension (D_p) of green body by 3D measurement module at 30 X, which is used to evaluate the formability. The hardness of the sintered ceramic was tested by digital microhardness tester (HVS-1000ZCM-XY, Shanghai Suoyan Testing Instrument Co., Ltd, China), 20 indentation points were taken, and the pressure was maintained at 196 N for 15 s. The density of sintered ceramic was measured by Archimedes drainage method. The zeiss sigma HD (Sigma 500, Carl Zeiss (Shanghai) Co., USA) was used to study the microstructure of the parts.

The flow process of photosensitive ceramic slurry obeys Herschel–Bulkley model [28] shown in formula 1. The static stress (σ_y^{Sta}) and dynamic stress (σ_y^{Dyn}) of the slurry are one of the main factors affecting the flow. In this study, the flow cycle curve is used to obtain the σ_y^{Dyn} and σ_y^{Sta}, as shown in Fig. 1.

$$\sigma = \sigma_y^{\mathrm{Dyn}} + \mathrm{K}\dot{\gamma}^{\mathrm{n}} \quad (1)$$

where: σ is the stress (Pa), σ_y^{Dyn} is the dynamic yield stress (Pa), K is the model coefficient, $\dot{\gamma}$ is shear rate s^{-1}), and n is the flow index.

Figure 2 shows the 3 stages of the cyclic flow of the ceramic slurry. A stress is applied (first stage) to overcome the static stress (σ_y^{Sta}) until slurry began to steady flow (second stage) through the round nozzle at a certain shear rate. The value of σ_y^{Sat} was obtained at the slope change of the stress vs. shear rate curve, which is fitted using the measured data. When the printing complete, the stress relaxed gradually to the σ_y^{Dyn} (third stage). The value of

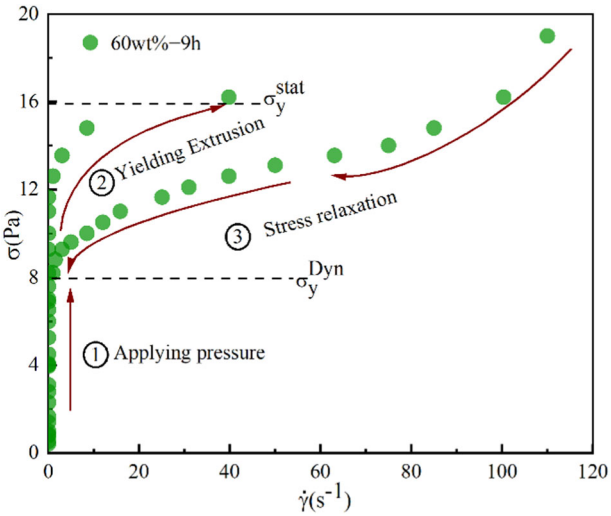

Fig. 2 Stress vs. shear rate cyclic flow curve of 60wt % slurry aged for 9 h. While measuring $\dot{\gamma}$, an increasing stress controlled ramp was applied ① until slurry yields at the static stress (σ_y^{Sta}) ②. While measuring stress, a decreasing shear rate controlled ramp was applied from $\dot{\gamma} = 120$ s^{-1} to $\dot{\gamma} = 1$ s^{-1}, until stress relaxes at σ_y^{Dyn} value ③

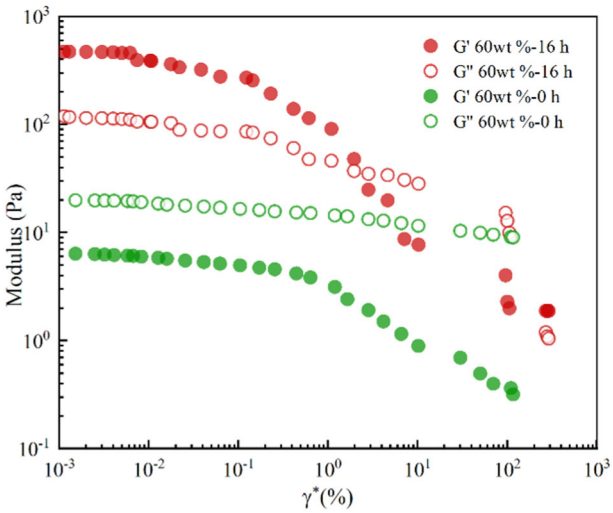

Fig. 3 Modulus vs. strain curve of 60wt % slurries after aging for 0 h and 16 h. The Modulus obtained by amplitude sweep at 1 Hz and (0.1–σ_y) Pa in range of (0.1–σ_y) Pa

σ_y^{Dyn} was obtained at the y-intercept by fitting the measured data brought into the Herschel–Bulkley model.

3 Results and discussion

3.1 Rheology of photosensitive ceramic slurry

To study the flow behavior of photosensitive ceramic slurry, the modulus vs. strain curve of 60wt % slurries at $t_{aging} = 0$ h and $t_{aging} = 16$ h in steady state were obtained, as shown in Fig. 3.

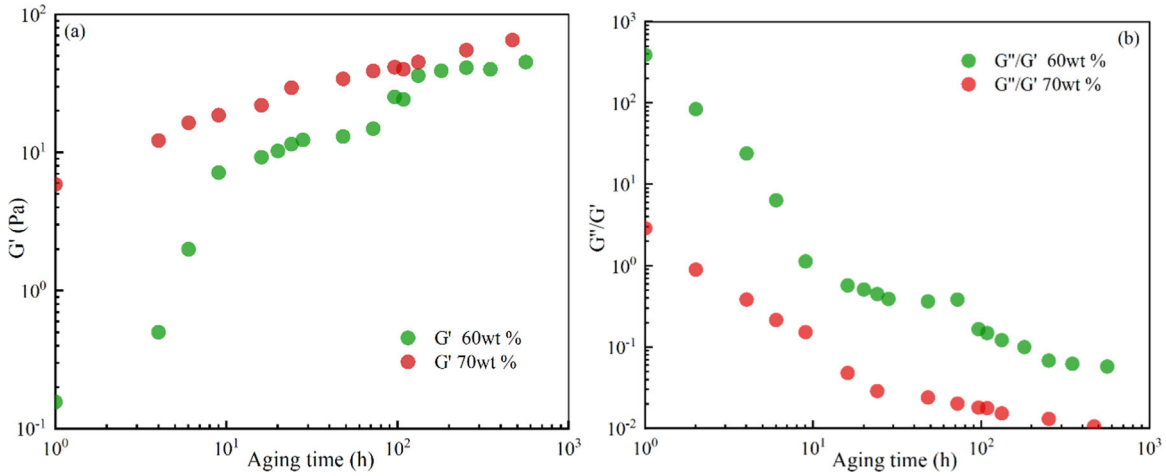

Fig. 4 The 60wt % and 70wt % slurries were measured at 1 Hz, (**a**) Evolution of G' with the aging time, (**b**) Evolution of G''/G' with the aging time

Figure 3 shows that photosensitive ceramic slurry was a viscoelastic fluid with complex shear modulus, including viscous modulus (G'') and elastic modulus (G'). The shear modulus decreases with the increase of strain (γ*). For slurry at $t_{aging} = 0$ h, the G'' of the slurry is greater than the G', and the slurry appears liquid. After aged 16 h, G'' is equal to G' when γ* is 2%, which is the mark of gelation and viscoelastic response. When the γ* is less than 2% and G'' is greater than G', the slurry is liquid and shows linear viscoelastic rheology. When the γ* is greater than 2 %, the slurry G'' is lower than G', and the slurry is solid and shows nonlinear viscoelastic rheology. The above results show that the photosensitive ceramic slurry has the general fluidity of a viscoelastic fluid, and the viscoelastic modulus of the slurry is affected by aging time. In order to further study the flow characteristics of photosensitive ceramic slurries, we characterized the G'' and G' of 60wt % and 70wt % slurries aged for 0–480 h, as shown in Fig. 4.

Figure 4a shows that the G' for both slurries increased with aged. For 60wt % slurry, when the aging time goes from 1 h to 9 h, the G' increased by nearly two orders of magnitude. For 70wt % slurry, the G' was always higher than 60wt % slurry. Figure 4b shows the ratio G''/G' of slurry at different aging time, where $G''/G' = 1$ is defined gel point. The 60wt % slurry reaches the gel point after 9 h while 70wt % slurry only needs 2 h. The G''/G' of the two kinds of slurry decreased with aging time, tending to remain relatively stable after 9 h of aging time, and the value of G''/G' with 70wt % slurry was always lower than 60wt % during the whole aging time. The results show that the slurry flow behavior turns to relatively stable when the aging time exceeds the gel point. And the lower the solid content of slurry, the greater the viscosity, and the more significantly affected by the aging time.

For 60wt % and 70wt % photosensitive ceramic slurry, when the aging time is greater than 9 h and 2 h respectively, meet the following Eq. 2:

$$\begin{cases} \varphi \geq 0.3 \\ G' \geq G'' \end{cases} \tag{2}$$

Theoretically, the flow process of the slurry obeys the Herschel–Bulkley model.

In order to further verify the slurry flow process after the gel obey the Herschel–Bulkley model, the evolution of viscosity (η) and stress (σ) with shear rate ($\dot{\gamma}$) of 60wt % and 70 wt% slurry at different aging time are obtained, as shown in Fig. 5.

Figure 5a shows a log–log plot of viscosity (η) vs. shear rate ($\dot{\gamma}$). For the 60wt % slurry (red lines), η is independent from $\dot{\gamma}$ at $t_{aging} = 0$ h, indicating a Newtonian behaviour (slope = 0). The 70wt % slurry (green hollow circles) exhibits a shear-thinning behaviour at $t_{aging} = 0$ h, with a shear-thinning index (proportional to the slope) lower than after gelation. Zero-shear viscosity values increase from 10^3 to 10^5 mPa·s with time. The 60wt % gel also progressively becomes a shear-thinning fluid, until gelation point, where a yield stress appears (Herschel–Bulkley model). After gelation, there is no increase in shear-thinning behaviour, since all slopes are equal and proportional to $\dot{\gamma}^{n-1}$ ($n \sim 0.5$) despite increasing viscosity. This shows that solid content has no effect on shear-thinning, which can be seen from the same slope of 70wt % and 60wt % gel in Fig. 5a. Figure 5b shows a log–log plot of stress (σ) vs. shear rate ($\dot{\gamma}$). For 60wt % slurry, log(σ) increases with aging time and is linear with log ($\dot{\gamma}$). For 60wt % slurry exceeding the gel point, the plot slope is basically the same. This is the same as expected by logarithmic linearization in Herschel–Bulkley equation, the

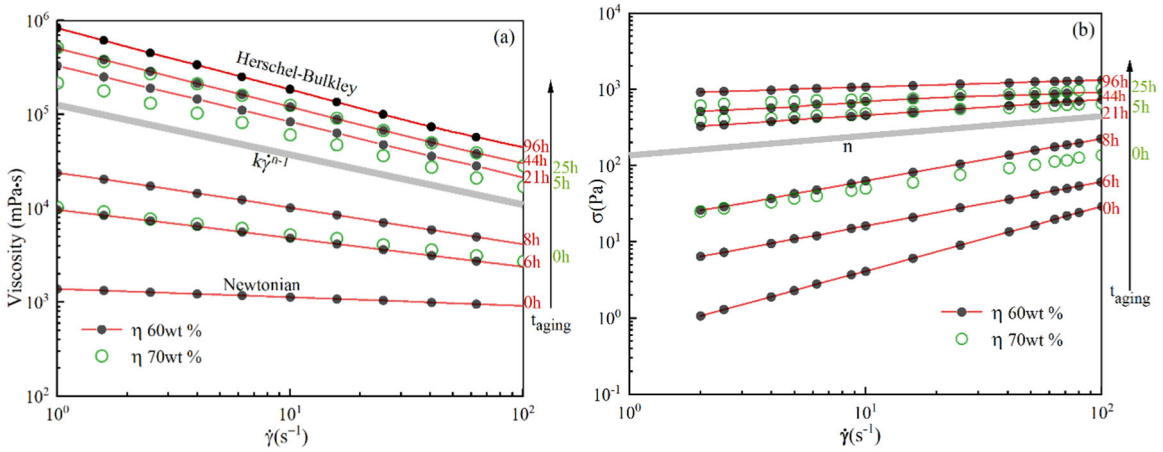

Fig. 5 **a** Evolution of viscosity (η) with shear rate ($\dot{\gamma}$), (**b**) Evolution of stress (σ) with shear rate ($\dot{\gamma}$). Respectively at $t_{aging} = 0$, 6, 8, 21, 44, 96 h and $t = 0$, 5, 25 h, from bottom to top for two plots

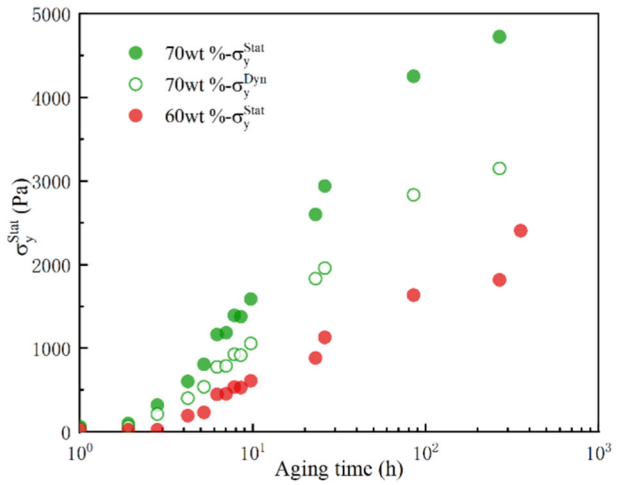

Fig. 6 Logarithmic plots of yield stress vs. aging time for 60wt % and 70wt % slurries

grey line represents the constant slope n, with no increase in shear-thinning effect after gelation.

In summary, two kinds of solid content slurries show shear-thinning behaviour for beyond the gelation time. In other words, the flow of the slurry after the gel time is in accordance with the Herschel–Bulkley model.

The σ_y^{Dyn} and σ_y^{Sta} play an important role in the flow process, and the rheology of the slurry is affected by the aging time, it is necessary to characterize the σ_y^{Dyn} and σ_y^{Sta} of 60wt % and 70wt % slurry under different aging time, as shown in Fig. 6.

Figure 6 shows the variation of σ_y^{Stat} and σ_y^{Dyn} of 60wt % and 70wt % slurries with $\dot{\gamma}$ under different aging time, which could be divided into two regions according to the variation trend, corresponding to the regions before and beyond the gel point in Fig. 4b respectively. In the region before the gel point, the liquid behavior of slurry manifests as Newtonian fluid, and the σ is implicit in the flow process. In the region after the gel point, the σ increases linearly as a function of log (t_{aging}). For 60wt % slurry, the difference between σ_y^{Stat} and σ_y^{Dyn} before the gel point ($t_{aging} = 9$ h) is small, and beyond the gel point, σ_y^{Stat} is always greater than σ_y^{Dyn}. For σ_y^{Stat}, that of the 70wt % slurry is always greater than 60wt %, which is due to the increase of van der Waals interaction force caused by excessive OA-modified Al_2O_3 particles [27], and leads to the overlapping of hydrocarbon long chains (–OOC–R) adsorbed on the surface of Al_2O_3 particles [28]. Once the slurry is still, the stress is relaxed, and the undamaged electrostatic bond between the particles remains the rest σ_y^{Dyn}.

The σ of UV-curable ceramic slurry deposited must overcome gravity and surface tension to remain the shape of printing parts. In fact, ceramic parts usually have different degrees of collapse deformation, and can't be controlled by the rheology of the slurry.

3.2 Formability

The formability of 3D printed ceramic parts is a key factor to the application performance. To study formability of MEX-PPM process, the ceramic green body was printed with different nozzle under different radiant power, as shown in Fig. 7. The printing direction circulated from left to right, and the printing speed was 5 mm/s. To simplify the comprehensive forming model, the above samples are printed in a single layer, and the formability of the green body is evaluated by the section dimensions in the length and height directions.

Figure 7 shows that the sample printed with low-aging slurry in the first row have higher collapse deformation at zero radiation power ($P = 0$ J/s), and the sample width is larger than the design dimension (D_d). Moreover, the

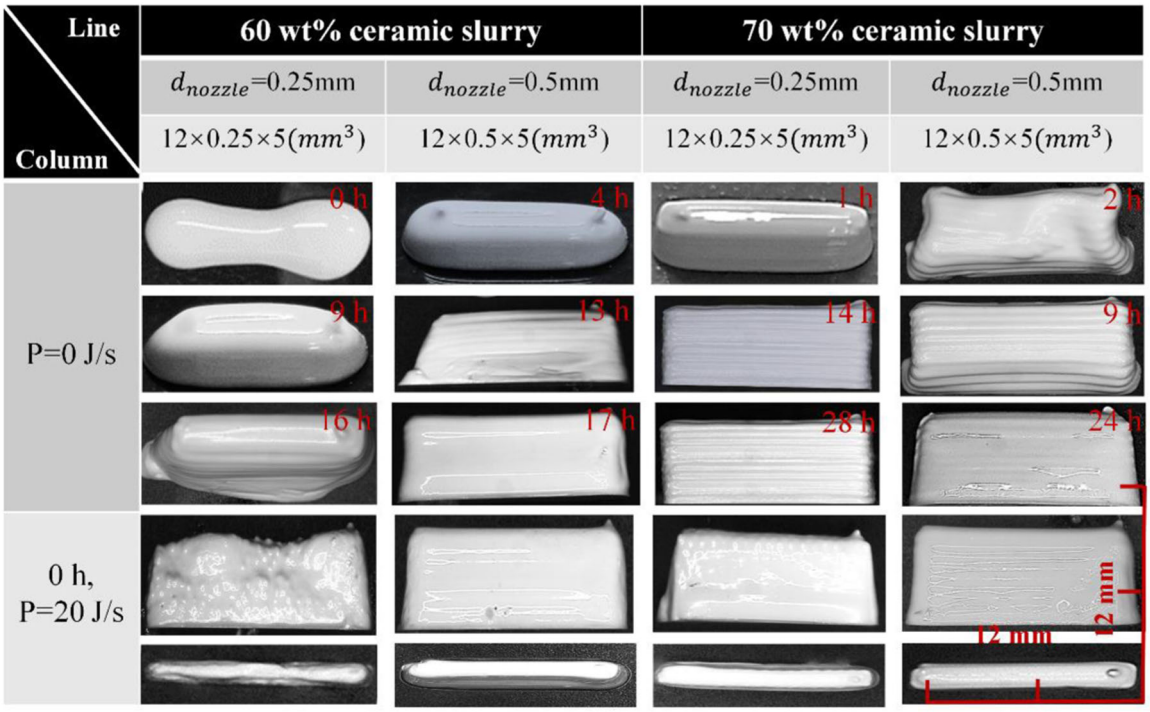

Fig. 7 Samples obtained from aged 60wt % and 70wt % slurry were printed with 0.25 mm and 0.5 mm diameter nozzles at speed of 5 mm/s

sample with 60wt % is droplet-shaped, which means it is difficult to maintain the sample structure. In the second row, the printed sample after the aging time has passed the yield point ($t_{aging} \geq 9$ h) was better to the first row. In the third row, the deformation of the sample decreases with aging time, but the sample of 60wt % slurry printed with 0.25 mm diameter nozzle still produces a certain deformation. The slurries in fourth row have the same ageing time as the first row but with UV curing. The radiation power provided during the printing process is 20 J/s. Comparing to the samples shown in rows from the first to the third, the samples under radiant power of 20 J/s during the printing process have improved formability in both height direction (the fourth row) and length direction (the fifth row). The green body dimension obtained by printing 70wt % slurry with 0.5 mm diameter nozzle is 12.03 mm × 5.11 mm (length x height) is close to the D_d (The first on the left of the fourth row). The surface quality of the green body printed by the nozzle with a diameter of 0.25 mm is poor, and the D_{pre} is far away from the D_d, which is caused by the excessive radiation power. The above experiments clearly prove that the radiation power by UV light can regulate the deformation caused by slurry rheology. However, how much radiant power is needed for the deformation during printing to achieve the perfect printing of parts? It is necessary to find out the relationship between the forming dimension of parts, rheology of ceramic slurry, process parameter such as printing speed and radiation power.

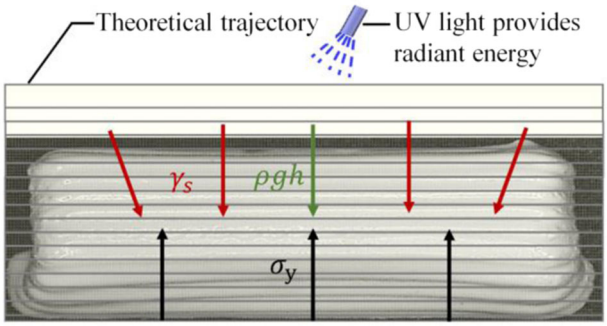

Fig. 8 Synergy of rheology and photo-polymerization behavior

3.3 Linking rheology, process parameters and formability

The printed green body by MEX-PPM is affected by gravity (ρgh), surface tension (γ_s), yield force (σ) and UV light radiation energy, as shown in Fig. 8.

In Fig. 8, the green arrow represents the gravity, and its direction is vertically downward. The red arrows represent the surface tension of the green body, and its direction points inward. The black arrows stand for the yield force of the slurry, and its direction is opposite to the resultant direction of gravity and surface tension.

According to the law of conservation of energy, the deformation of the sample produced by the action of γ_s, and σ^{Dyn} and ρgh can be compensated by the radiation energy

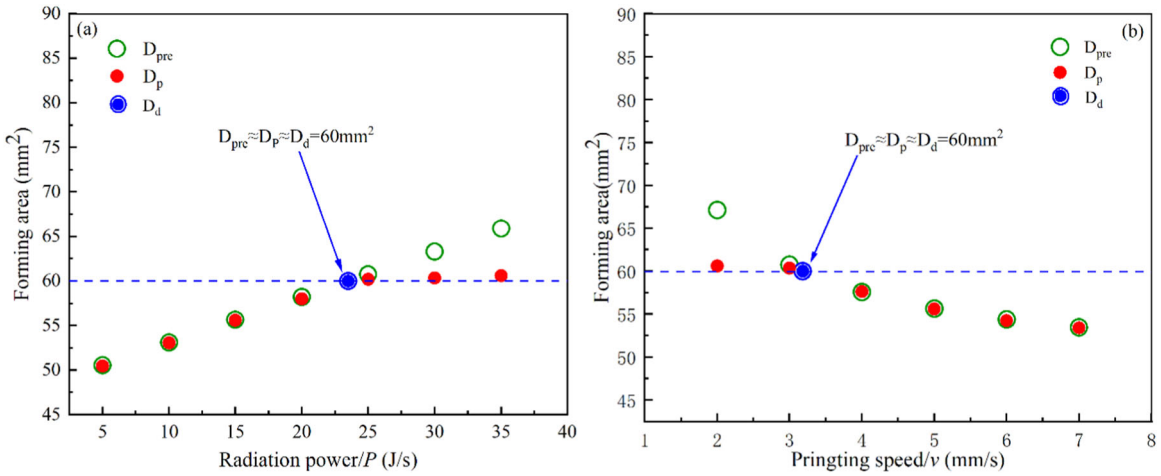

Fig. 9 The deformation of the ceramic green body printed with 70wt % slurry at $t_{aging} = 0$. **a** The radiation power (P) is the variable, and the printing speed (v) is 5 mm/s. **b** The printing speed (v) is the variable, and the radiation power (P) is 15 J/s

provided by MEX-PPM process, thereby forming a satisfactory part dimension, as shown in formula (3) [29].

$$\left(\sigma^{Dyn} - \rho g h + 2 * \gamma_s * \mathrm{d_{nozzle}}^{-1}\right) * \left(\Delta D * \mathrm{d_{nozzle}}^{-1}\right) = P_n \tag{3}$$

where d_{nozzle} is the diameter of nozzle, $\Delta D = D_{pre} - D_0$ is the deformation of the printed sample, D_{pre} is theoretical printed dimension of the green body, is also predicted dimension. D_0 is the printed dimension (D_0) at $P_n = 0$, P_n is the radiation energy required to meet the forming dimensions. The radiated energy depends on the radiated area and energy density, which can be calculated by formula (4) [30].

$$P_n = E * D_{pre} = \frac{2 * P * D_{pre}}{\pi * \omega_0 * \nu} \tag{4}$$

where P is the radiation energy per unit time, is also radiation power, ω_0 is spot diameter, ν is printing scanning speed, E is the radiation energy density.

By extending formulas (3) and (4), the forming dimensions model is a function of the P, ω_0, ν, d_{nozzle}, the dimension of the parts (h, D_{pre}) and material properties (σ^{Dyn}, ρ, γ_s), as shown in formula (5).

$$D_{\mathrm{pre}} = \frac{\mathrm{D_0} * \pi * \omega_0 * \nu * \left(\sigma^{Dyn} - \rho * g * h - 2 * \gamma_s * d_{nozzle}^{-1}\right)}{\pi * \omega_0 * \nu * \left(\sigma^{Dyn} - \rho * \mathrm{g} * h - 2 * \gamma_s * d_{nozzle}^{-1}\right) - 2 * \mathrm{P} * d_{nozzle}}, \ \sigma^{Dyn} - \rho g h + 2 * \gamma_s * \mathrm{d_{nozzle}}^{-1} \neq 0 \tag{5}$$

where: γ_s and σ^{Dyn} can be measured directly, $g = 9.8\ \mathrm{g/cm^3}$.

According to the comprehensive forming model of sample (formula (5)), when printing parts with a specific solid content and dimension, the h, D_0 and $\rho g h$ are constant values. In addition to adjusting the rheological properties (σ^{Dyn}, γ_s) of slurry, the process parameters (P, v) can also be directly controlled to increase the formability of ceramic part. As shown in Fig. 6, the actual deformation of the first green body on the right of the fourth row is 0.3 mm × 0.11 mm relative to the design dimension (D_d) (12 mm × 5 mm). According to the comprehensive forming model, for 70wt % slurry at $t_{aging} = 0$, the printing speed and radiation power are respectively regulated to 5 mm/s and 23.5 J/s, the perfect forming of green body can be realized through 0.5 mm nozzle.

3.4 Effectiveness of comprehensive forming model

Through preliminary printing experiments, the 70wt % slurry can be smoothly passed with a nozzle of more than 0.3 mm. The filament can be perfectly extruded at a printing speed of 2–7 mm/s, and the spot diameter is close to the nozzle diameter, the printed sample has good interlayer bonding.

Therefore, for the image of the green body in Fig. 7, the printing speed and radiation power can be adjusted according to the comprehensive forming model to improve the formability of the green body. The results of regulation are shown in the Fig. 9.

In Fig. 9, the green hollow dots corresponds to the D_{pre} calculated according to the comprehensive forming model, and the red solid dot corresponds to the printed dimension (D_p). When the D_{pre} and D_p are close to the D_d, the blue dot appears. In Fig. 9a, the radiation power is in the range of 5 J/s ≤ P < 23.5 J/s, the D_p is close to the D_{pre}, and they gradually approach the D_d with the increase of radiation power. When $P = 23.5$ J/s, the D_p, D_{pre} and D_d are approach. In Fig. 9b, the printing speed is in the range of 3.2 mm/s < v ≤ 7 mm/s, the D_p is close to the D_{pre}, and they gradually approach the D_d with the decrease of printing speed. When $v = 3.2$ mm/s, the three dimensions are close

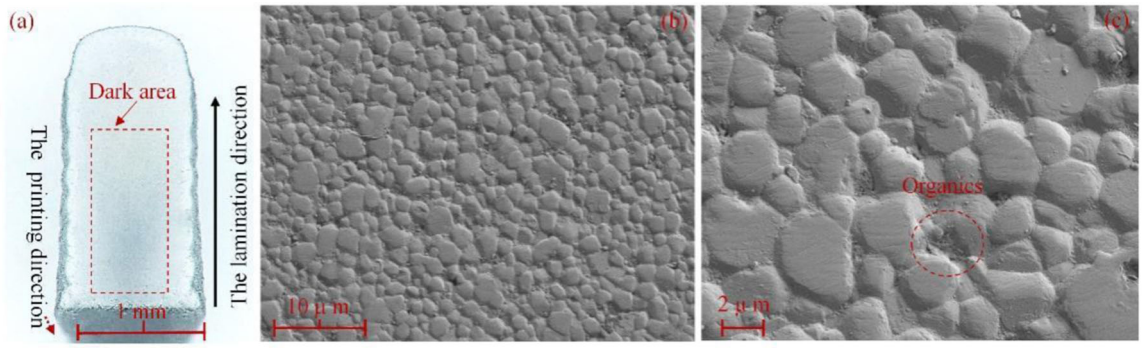

Fig. 10 Sintered body: (**a**) The cross section at printing direction. **b** The microstructure at the X500 magnification. **c** The microstructure at the X2000 magnification

to each other. This means that adjusting radiation power and printing speed can make up for the deformation caused by the weak yield stress of slurry rheology. The results show that the printing of green body can be well realized based on the comprehensive model regulation, and the forming dimension of the green body can be predicted according to the rheology of slurry, printing parameters such as printing speed and radiation power. However, when $P > 23.5$ J/s and $v < 3.2$ mm/s, the D_p is smaller than the D_{pre}, because the radiation power and printing speed exceed the limit value required by the forming dimension, resulting in invalid model dimension. The above problems can be solved by setting the upper and lower limits of the printing speed and radiation power in the comprehensive forming model. To achieve the printing that just maintains the shape of the deposition layer and the good adhesion between layers by adjusting the process parameters in a limited range.

The above research shows that the comprehensive model linking rheology of slurry, printing parameters and forming dimension can well realize the printing of ceramic green body. By changing the radiation power and printing speed, the deformation of green body caused by rheological behavior is compensated, and the formability of green body is improved. These results indicate that the comprehensive forming model of green body established is reliable when evaluating the formability of photosensitive ceramic slurry by MEX-PPM process.

3.5 Microstructure and mechanical properties

Figure 10 shows the microstructure of sintered body. The green body is formed by MEX-PPM process using 70wt % photosensitive ceramic slurry at printing speed of 5 mm/s and radiation power of 23.5 J/s which is the best process parameter controlled by comprehensive forming model.

Figure 10a is a cross section of the ceramic sintered body at printing direction. The surface of the cross section has obvious slurry stacking tracks, the internal structure of the cross section is uniform, and the slurry deposition layers are fused with each other, and there is no obvious filling track. The interior of the sintered body is gray-white, and the surface is black-gray, which is due to the decomposition of organic matter during the degreasing process, which overflows from the interior and adheres to the surface of the sintered body. Figure 10b shows the microstructure at X500 magnification. The internal Al_2O_3 particles are uniformly arranged without visible pores, but there are a small amount of debris between the Al_2O_3 particles. Figure 10c shows the microstructure at X2000 magnification. The organics has not completely overflowed, which is consistent with the dark gray area in Fig. 10a. These problems can be avoided by fully degreasing, which can further improve the compactness and mechanical properties of ceramics.

In addition, the same batch of 20 parts were tested for relative density and hardness, the average relative density reached 96.2 % of the theoretical density of Al_2O_3 (3.96 g/cm^3), and the average hardness was 15.67 GPa. The above results show that the ceramic parts produced by adjusting the MEX-PPM process parameters according to the comprehensive forming model also have good quality. Even though these values are moderately reliable and restrictive, the forming quality of the product obtained is better than that of the reported values of both MEX and PPM process under the same conditions.

4 Conclusion

In this work, a series of 60wt % and 70wt % ceramic slurries were prepared using spherical alumina powder with particle size of 1 μm, prepolymer 1, 6-hexanediol diacrylate, surfactant oleic acid and photo-initiator diphenyl (2, 4, 6-trimethylbenzoyl) phosphate oxide as raw material. The rheology of photosensitive ceramic slurry was researched, the deformation of green body printed by MEX-PPM process was evaluated, and the comprehensive forming model

including the dimension of green body, rheology of slurry and MEX-PPM process parameter such as printing speed and radiation power was established. It was concluded that the deformation of the green body caused by rheology of slurry could be compensated by adjusting process parameters based on the model. The printing speed and radiation power are respectively regulated to 5 mm/s and 23.5 J/s, and the D_p of the green body using 70wt % photosensitive ceramic slurry is approximately the D_{pre} and D_d. The sintered body internal structure of ceramic part is dense and uniform, the relative density reaches at 96.2% (theoretical density of 3.96 g/cm^3), and the hardness reaches at 15.67 GPa. In sum, the proposed comprehensive model could be used to guide the production of dense ceramic parts with low deformation, profitable in reasonable and convenient design of ceramic slurry and adjustment of process parameters, providing material basis and technical support for 3D printing ceramic technology.

Author contributions All authors contributed to the study conception and design. Material preparation, data collection, and analysis were performed by X.H., J.X. and W.J. The first draft of the manuscript was written by X.H. In the process of manuscript revision, X.H. and J.X. prepared materials, collected data and analyzed, revised the manuscript, and got the final manuscript. All authors read and approved the final manuscript.

Funding information This research was funded by the National Natural Science Foundation of China (51805212), Natural Science Found of Jiangsu Province (BK20160182) and the Major Scientific and the Technological Innovation Project of Shandong Province [2019JZZY020111].

Compliance with ethical standards

Conflict of interest The authors declare no competing interests.

References

1. Gong G, Ye J, Chi Y, Zhao Z, Wang Z, Xia G, Du X, Tian H, Yu H, Chen C (2021) Beyond proteins: ubiquitylation of lipopolysaccharide to fight bacteria. Mater Res Technol 15:855–884
2. Mao M, He J, Li X, Zhang B, Lei Q, Liu Y, Li D (2017) The emerging frontiers and applications of high-resolution 3D printing. MIcromachines-Basel 8:113
3. Jain K, Shukla R, Yadav A, Ujjwal RR, Flora SJS (2021) 3D printing in development of nanomedicines. Nanomaterials (Basel) 11:420
4. Lu B, Li D, Tian X (2015) Development trends in additive manufacturing and 3D printing. Engineering 1:085–089
5. Bingheng L (2020) New acoustoelastic effect characterization method for acoustic reflection and transmission coefficient of prestressed thin plate at liquid-solid interface. China Mech Eng 31:19–23
6. Pham DT, Gault RS (1998) A comparison of rapid prototyping technologies. Int J Mach Tools Manuf 38:1257–1287
7. Liu G, Zhang X, Chen X, He Y, Cheng L, Huo M, Yin J, Hao F, Chen S, Wang P, Yi S, Wan L, Mao Z, Chen Z, Wang X, Cao Z, Lu J (2021) Additive manufacturing of structural materials. Mater Sci Eng: R: Rep. 145:100596
8. Li S, Duan W, Zhao T, Han W, Wang L, Dou R, Wang G (2018) The fabrication of SiBCN ceramic components from preceramic polymers by digital light processing (DLP) 3D printing technology. J Eur Ceram Soc 38:4597–4603
9. Kumar P, Mahamani A, Prasad BD (2020) Additive manufacturing - a literature review. Mater Sci Forum 979:74–83
10. Chen Z, Li Z, Li J, Liu C, Lao C, Fu Y, Liu C, Li Y, Wang P, He Y (2019) 3D printing of ceramics: a review. J Eur Ceram Soc 39:661–687
11. Koopmann J, Voigt J, Niendorf T (2019) Additive manufacturing of a steel–ceramic multi-material by selective laser melting. Metall Mater Trans B 50:1042–1051
12. Ju Y, Ha J, Song Y, Yun JS, Lee D (2020) Optimizing the printability and dispersibility of functionalized zirconium oxide/acrylate composites with various nano-to micro-particle ratios. Ceram Int 46:26903–26910
13. Ketel S, Falzone G, Wang B, Washburn N, Sant G (2019) A printability index for linking slurry rheology to the geometrical attributes of 3D-printed components. Cem Concr Compos 101:32–43
14. Liu W, Li M, Nie J, Wang C, Li W, Xing Z (2020) Synergy of solid loading and printability of ceramic paste for optimized properties of alumina via stereolithography-based 3D printing. Mater Res Technol 9:11476–11483
15. Liu Z, Bhandari B, Prakash S, Mantihal S, Zhang M (2019) Linking rheology and printability of a multicomponent gel system of carrageenan-xanthan-starch in extrusion based additive manufacturing. Food Hydrocoll 87:413–424
16. Chen J, Bao E, Huang D, Ding Y, Qiu X (2020) FKBP51 induces p53-dependent apoptosis and enhances drug sensitivity of human non-small-cell lung cancer cells. Mater Trans 61:2236–2240
17. Feilden E, Blanca EG-T, Giuliani F, Saiz E, Vandeperre L (2016) Robocasting of structural ceramic parts with hydrogel inks. J Eur Ceram Soc 36:2525–2533
18. Pierin G, Grotta C, Colombo P, Mattevi C (2016) Direct Ink Writing of micrometric SiOC ceramic structures using a preceramic polymer. J Eur Ceram Soc 36:1589–1594
19. He R, Liu W, Wu Z, An D, Huang M, Wu H, Jiang Q, Ji X, Wu S, Xie Z (2018) Fabrication of complex-shaped zirconia ceramic parts via a DLP- stereolithography-based 3D printing method. Ceram Int 44:3412–3416
20. Hwa LC, Rajoo S, Noor AM, Ahmad N, Uday MB (2017) Recent advances in 3D printing of porous ceramics: a review. Curr Opin Solid St M 21:323–347
21. Wang M, Xie C, He R, Ding G, Zhang K, Wang G, Fang D (2019) Polymer-derived silicon nitride ceramics by digital light processing based additive manufacturing. J Am Ceram Soc 102:5117–5126
22. He X, Xu J, Ji W (2021) Evaluation of a novel laboratory candiduria screening protocol in the intensive care unit. J Ceram Soc JPN 129:489–495
23. M'barki A, Bocquet L, Stevenson A (2017) Linking rheology and printability for dense and strong ceramics by direct ink writing. Sci Rep 7:10
24. Li X, Hu K, Lu Z (2019) Healthcare simulation in China: current status and perspectives. J Eur Ceram Soc 39:2503–2509
25. Chen ZW, Li JJ, Liu CB, Liu Y, Zhu JY, Lao CS (2019) Preparation of high solid loading and low viscosity ceramic slurries for photopolymerization-based 3D printing. Ceram Int 45:11549–11557
26. Rosa M, Barou C, Esposito V (2018) Zirconia UV-curable colloids for additive manufacturing via hybrid inkjet printing-stereolithography. Mater Lett 215:214–217
27. Barnes, HA (1992) China Petrochemical Press, 9

28. Yao YJ, Qiu T, Yang CH (2009) Polymorphic Alu insertions and their associations with MHC class I alleles and haplotypes in Han and Jinuo populations in Yunnan Province, southwest of China. China Ceram 4:51–54
29. Ye WG, Yu GX (2012) Tsinghua University Press, 12
30. Li KH, Zhao Z (2017) The effect of the surfactants on the formulation of UV-curable SLA alumina suspension. Ceram Int 43:4761–4767